

Original Research

Establishment of Ferroptosis-Associated Molecular Subtypes and Hub Genes Related to the Immune Microenvironment of Heart Failure

Jiabin Zhou^{1,2,†}, Jiayu Shi^{1,†}, Peng Xu^{1,2,†}, Gujie Wu^{2,3}, Chen Wang^{1,2}, Jingyu Li^{1,2}, Hanrui Sun^{1,2}, Weiming Yan^{1,2}, Qi Lu^{1,2,*}¹Department of Cardiology, Affiliated Hospital of Nantong University, 226000 Nantong, Jiangsu, China²Medical School, Nantong University, 226000 Nantong, Jiangsu, China³Department of Cardiovascular Surgery, Affiliated Hospital of Nantong University, 226000 Nantong, Jiangsu, China*Correspondence: luqint@sina.com (Qi Lu)

†These authors contributed equally.

Academic Editor: Rajesh Katare

Submitted: 1 March 2023 Revised: 18 April 2023 Accepted: 26 April 2023 Published: 19 October 2023

Abstract

Background: Ferroptosis is a form of iron-dependent regulated cell death, and prior work has highlighted the potential utility of ferroptosis-inducing agents as tools to treat heart failure (HF). To date, however, no detailed examinations of the prognostic utility of ferroptosis-related genes (FRGs) in HF have been conducted. **Methods:** We used established genomic identification of FRGs for total samples in the gene expression omnibus (GEO) database, screened for differentially expressed FRGs, performed protein-protein interaction analysis and functional analysis of HF immune microenvironment subtypes. Subsequently, we applied tools to calculate immune cell infiltration, compare immune cell, immune response genomic and *HLA* gene differences between subtypes, and perform candidate drug identification. Finally, preliminary *in vivo* validation of the screened central genes was performed in animal models. **Results:** FRGs were compared between samples from HF and healthy control donors, revealing 62 of these genes to be differentially expressed as a function of HF status. HF patient-derived tissues exhibited significant changes in the expression of *HLA* genes, increase immune cell infiltration, and higher levels of other immune-related genes within the associated immune microenvironment. These FRGs were then leveraged to establish two different immune-related subtypes of HF based on clustering analysis results, after which these subtypes were characterized in further detail. Functional enrichment analyses revealed the identified differentially expressed genes to be enriched in key immune-related pathways including the primary immunodeficiency, natural killer cell-mediated cytotoxicity, FcεRI signaling, and antigen processing and presentation pathways. The impact of the immune microenvironment was also explored through functional analyses, core gene analyses, and efforts to identify potential drug candidates for HF patients. Moreover, four key hub genes were identified as promising targets for therapeutic intervention in HF, including *HDAC1*, *LNPEP*, *PSMA1*, and *PSMA6*. Subsequent preclinical work in a mouse model system supported a potential role for HDAC1 as an important biomarker associated with the incidence of HF. **Conclusions:** To sum up, these results emphasize the importance of ferroptosis as a regulator of the HF-related immune microenvironment, highlighting viable avenues for the further study of molecular targets amenable to pharmacological intervention with the aim of treating this debilitating disease.

Keywords: heart failure; ferroptosis-related gene; molecular subtype; immune microenvironment; hub gene; drug

1. Introduction

Heart failure (HF) remains a major threat to global public health, affecting approximately 64.3 million individuals and necessitating consistent and systematic management to ensure optimal patient outcomes [1]. Measurements of key circulating biomarkers have been shown to be strongly correlated with the clinical prognosis of HF patients [2], and international guidelines have recommended the use of a range of biomarkers as guides to gauge HF patient outcomes including N-terminal pro-B type natriuretic peptide (NT-proBNP) and high-sensitivity troponin T (hs-cTNT) [3]. Traditional biomarker assays are inexpensive and straightforward, enabling the routine evaluation of patients with the goal of cost-effectively identifying individuals at high risk without the need for invasive procedures or

expensive instrumentation, thereby allowing these individuals to receive further personalized care [4]. The establishment of a more detailed understanding of key biomarkers associated with HF may represent a means of more rationally and effectively facilitating patient risk stratification.

Ferroptosis is a form of regulated cell death that differs from apoptotic or necrotic processes [5], occurring due to the iron-mediated accumulation of lipid peroxides within affected cells [6]. The induction of ferroptosis holds promise as a therapeutic strategy in certain diseases, including in HF patients that have responded poorly to more traditional forms of clinical management [7–9]. Prior work has revealed a range of genes that regulate ferroptosis in positive or negative manners [10,11], but the relationships between these different genes and the prognosis of HF patients



has yet to be clarified. Efforts to more clearly define the molecular etiology of ferroptosis-related genes (FRGs) in the pathogenesis of HF may thus aid in clarifying the heterogeneous phenotypes observed among HF patients, thereby revealing new opportunities to provide affected individuals with more efficacious care.

For the present study, a series of analyses of gene expression profiles and microarray-derived data were used to compare transcriptomic differences between HF patients and healthy controls with the goal of defining key FRGs that are differentially expressed as a function of HF status and to define hub biomarkers of HF-related immunoregulation. Together this research effort will advance current understanding of the molecular factors that drive HF at the systems biology level.

2. Material and Methods

2.1 Data Sources

Microarray data used for this study included the GSE57338 dataset (<https://www.ncbi.nlm.nih.gov/geo/query/acc.cgi?acc=GSE57338>), which included 313 total samples (177 diseased samples, 136 control samples). FRGs were identified using established gene sets including PMID: 33867820 ($n = 103$), PMID: 33767582 ($n = 386$), PMID: 32760210 ($n = 60$), and the FerrDb database ($n = 369$), yielding 449 total FRGs.

2.2 Protein-Protein Interaction Analyses

The 449 identified FRGs were used to generate a protein-protein interaction network (<https://string-db.org>), with the MCC algorithm in the CytoHubba v0.1 (New York City, NY, USA) plug-in being used to select hub genes from this network within the Cytoscape application for further downstream analyses.

2.3 Functional Analyses of HF Subtypes

Functional enrichment analyses for different HF immune-related subtypes were assessed based on enrichment scores for particular gene sets in individual samples as determined with a non-parametric unsupervised gene set variation analysis (GSVA) approach with the R GSVA v1.38 package (Bioconductor, Boston, MA, USA), which enables the transformation of gene expression data from individual genes in a characteristic expression matrix. Differential expression analyses were then performed with the R limma package (Bioconductor, Boston, MA, USA), with a false discovery rate (FDR) ≤ 0.05 being indicative of a significant difference.

2.4 Immune Infiltration Analysis

There are several tools to calculate immune cell infiltration, such as CIBERSORT, XCELL, SSGSEA, TIMER, etc. To avoid the limitations of the database and to improve the accuracy of the data analysis results, we applied here at least three tools to calculate immune cell infiltration, com-

paring immune cells between subtypes, immune response gene sets, and *HLA* gene differences.

2.5 Candidate Drug Identification

Hub modules of interest were introduced into the DGIdb database to facilitate the identification of candidate gene-drug interactions, with the ggplot2 v3.3.4 R package (Hadley Wickham, London, UK) being used to generate a Sankey map with geom alluvium as a means of highlighting the associations between hub genes and drug candidates.

2.6 Reagents

Primary antibodies specific for HDAC1, LNPEP, PSMA1 and PSMA6 were from ABclonal (A19571, A11959, A3460, and A2188), while antibodies specific for β -actin as well as secondary goat anti-rabbit IgG were from Wuhan Servicebio Technology Co., Ltd. (GB15003 and GB23303, Wuhan, China). A test kit for measuring ferrous ion concentration (E-BC-K773-M) was purchased from Elabscience (Wuhan, China), and the kits for measuring malondialdehyde (MDA) and glutathione (GSH) levels were obtained from Nanjing Jiancheng Institute of Biological Engineering (A003-4-1, A006-2-1, Nanjing, China).

2.7 Mouse Model Studies

C57BL/6 mice (specific pathogen-free 8-week-old males, 20–25 g; Experimental Animal Center of Nantong University) were housed under standard conditions (21 ± 1 °C, 55–60% humidity) with ad libitum food and water. All animal research was approved by the Animal Ethics Committee of Nantong University in accordance with the Guide for the Care and Use of Laboratory Animals. Animals were randomly assigned to sham or transverse aortic constriction (TAC) surgical treatment groups ($n = 6$ each), with TAC-induced pressure overload then being modeled as reported previously. Following this surgical procedure, mice were monitored for 6 h, after which they were returned for standard feeding and care to the experimental animal center. In mice that underwent sham procedures, sutures were passed through the soft tissue located underneath the aortic arch without any corresponding ligation, while all other procedure steps were identical to those in mice that underwent the TAC procedure. Mice were monitored daily after surgical treatment and continued to have ad libitum food and water access.

Over 80% of the mice in both surgical groups survived, with comparable rates in both groups. Surviving mice underwent echocardiographic assessment 8 weeks after surgery, followed by further experimentally appropriate examination.

2.8 Transthoracic Echocardiography

Following isoflurane-mediated anesthetization, mice were fixed in the supine position on an operating table. The skin of the anterior thoracic region was then prepared,

coated with coupling agent, and a high-resolution small animal ultrasound imaging system (Vevo 2100, Visual Sonics, Canada) was used to conduct echocardiographic analyses of these animals using the FMS-250 probe (depth: 2.0–2.5 cm, frequency: 13–24 MHz). Under M-mode ultrasonographic visualization of cardiac structures in these animals, parameters measured using the left ventricular (LV) short-axis and parasternal LV long-axis views included LV internal diastolic diameter (LVIDd), LV internal diameter end-systole (LVIDs), and interventricular septal dimension in diastole (IVSd). LV systolic function-related indices were then computed based upon these values over an average of 3–5 cardiac cycles, including ejection fraction (EF) and fractional shortening (FS).

2.9 Histological Analysis

Mouse hearts were collected and fixed in 4% paraformaldehyde for 48 hours and embedded in paraffin. Next, the tissue was cut into 5 mm cross-sectional sections. The sections were stained with hematoxylin-eosin (HE) to observe the histopathological changes in the myocardium, WGA staining to measure the cross-sectional area of cardiomyocytes, and Masson staining to evaluate the extent of interstitial fibrosis in the mouse myocardium.

2.10 Transmission Electron Microscopy (TEM)

After collection, cardiac tissue samples were fixed for 10 min with 1% glutaraldehyde, followed by further fixation for 1 h at room temperature using 3% glutaraldehyde. Samples were then further fixed for an additional 1 h at room temperature using 1% osmium tetroxide in 0.1 mol/L dimethylarsinate buffer, followed by embedding in resin. Polymerized ultrathin sections were then stained using uranyl acetate and lead nitrate, followed by TEM imaging to assess mitochondrial morphology and transverse muscle arrangement.

2.11 Iron Ion Quantification

Cells were treated as above, and a bicinchoninic acid (BCA) kit was used to detect protein concentrations in sample lysates. A ferrous ion colorimetric test kit (E-BC-K773-M, Elabscience, Wuhan, China) was then used to detect iron ion levels based on provided directions. Briefly, the provided probe bound to ferrous ions released by cells, with the resultant absorbance at 593 nm being quantified to measure intracellular Fe^{2+} content.

2.12 Analyses of MDA and GSH Levels

After cells had been harvested and lysed, a BCA kit was used to measure protein concentrations. MDA levels in these cells were assessed using an MDA assay kit, with absorbance at 530 nm ultimately being measured. Similarly, GSH levels in these cells were analyzed based on the directions provided with a micro-reduced GSH assay kit.

Absorbance was assessed at 405 nm, and GSH levels were established based on a standard curve.

2.13 qPCR

RNA was isolated from cardiac tissue samples and cardiomyocytes with Trizol (Servicebio, Wuhan, China). HiScript II Q RT SuperMix (Vazyme, Nanjing, China) was used to prepare cDNA, after which ChamQ Universal SYBR qPCR Master Mix (Vazyme, Nanjing, China) and a fluorescent qPCR instrument (Bio-rad; CFX, CA, USA) were used for qPCR analyses. Primers used for this study (RiboBio, Guangzhou, China) had the following sequences: GAPDH: (F: CCTCGTCCCGTAGACAAAATG, R: TGAGGTCAATGAAGGGGTCGT); HDAC1: (F: TCATAAATACGGAGAGTACTTCCA, R: CGTCTCGCAGTGGGTAGTTCAC); LNPEP: (F: CAAACCAGTCAGCAGAACTCATC, R: TAGAGGAATAATGGCAGTGGGAAG); PSMA1: (F: CGGGTCTAACTGCTGATGCC, R: CATATCGCTGTGTTGGGATCTG); PSMA6: (F: GCAGAGATTGACGCTCACCTT, R: GGCCTCTATGATGTCAGTTTGTG). GAPDH was used as a control to normalize gene expression, with relative expression being measured using the $2^{-\Delta\Delta CT}$ method.

2.14 Western Immunoblotting

A protein extraction reagent was used to isolate proteins from tissue or cell samples, after which a BCA protein analysis kit (Servicebio, Wuhan, China) was used to measure protein concentrations. Proteins were then separated via 8% SDS-PAGE (Servicebio, Wuhan, China), transferred to polyvinylidene difluoride (PVDF) membranes, and blots were then blocked for 2 h at room temperature with 5% non-fat milk prior to incubation overnight with appropriate primary antibodies at 4 °C. Blots were rinsed with TBST three times, then probed with secondary antibodies for 2 h. Chemiluminescent reagents were then used to detect protein bands, followed by quantification using ImageJ V1.8.0 (National Institutes of Health, Bethesda, MD, USA).

2.15 Statistical Analysis

Data are reported as means \pm SEM, and were analyzed using GraphPad Prism 9.3.0 (GraphPad Software, San Diego, CA, USA). Differences between groups were compared via Student's *t*-tests or one-way ANOVAs with Bonferroni post hoc tests. $p < 0.05$ was the significance threshold.

3. Results

3.1 Exploration of the Heart Failure-Associated FRG Transcriptomic Landscape

To gain initial insight into the relationships between ferroptosis and HF, a comprehensive set of 449 FRGs with corresponding genomic location information was established (Fig. 1A). Protein-protein interaction analyses were

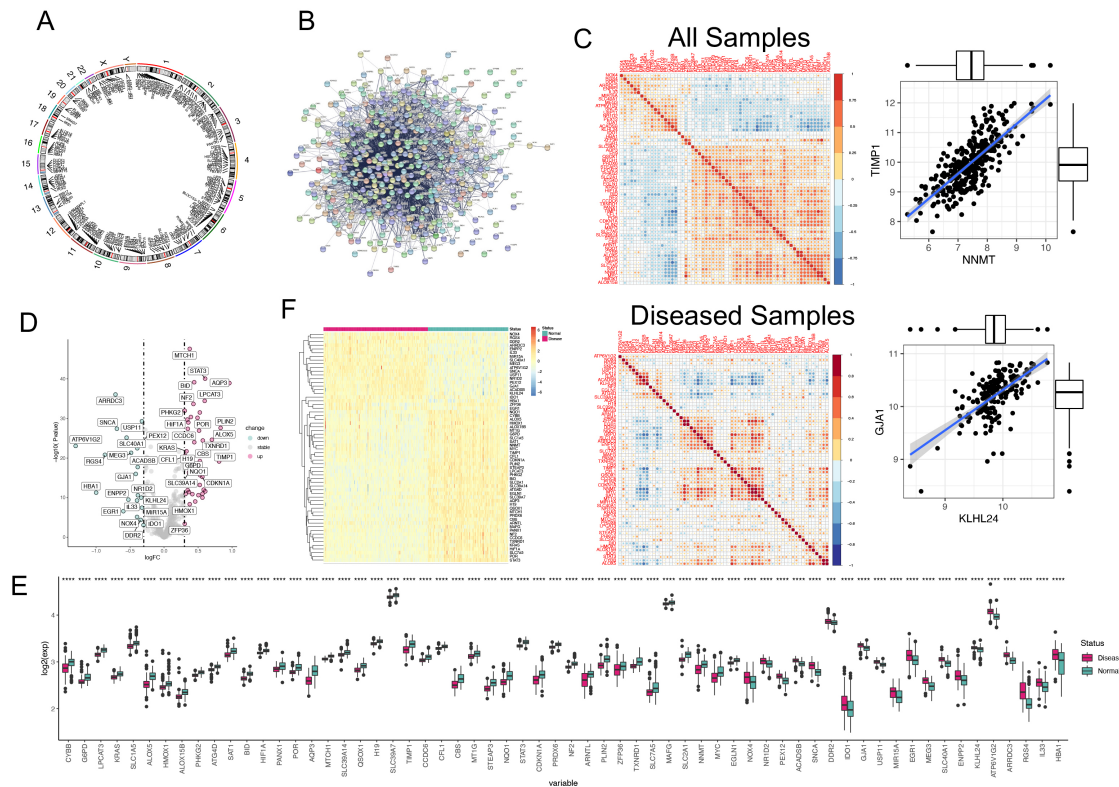


Fig. 1. Ferroptosis-related genes (FRGs) landscape in heart failure. (A) Genomic position configuration of 449 FRGs. (B) Protein-protein interactions of 449 FRGs. (C) Differential FRG expression correlations (Expression correlation analysis in all samples (top) and in disease samples (bottom), scatter plots showing expression of positively correlated FRGs in different samples). (D) volcano plot showing up- or down-regulation of FRGs in disease compared to control. (E) Box plot showing significant differences in genes in the samples. (F) Heat map showing the expression of FRGs in all samples.

also conducted for these FRGs (Fig. 1B). The relationship between these FRGs was then examined by comparing all samples in the selected microarray dataset to samples from HF patients (Fig. 1C). Differential FRG expression between healthy control individuals and HF patients was then compared using established cutoff criteria, revealing 62 differentially expressed FRGs of which 42 and 20 were respectively upregulated and downregulated in HF samples (Fig. 1D–F, **Supplementary Table 1**).

3.2 The Association between FRGs and Heart Failure-Related Immune Regulation

The immunological microenvironment of HF-related patient samples was next characterized. Analyses of the HLA expression profiles in these samples revealed significant downregulation of most HLA genes in HF samples relative to healthy tissues (Fig. 2A). Correlations between these HLA genes and the 62 identified differentially expressed FRGs were also examined (Fig. 2B). Immune infiltration analyses performed through three computational approaches revealed higher levels of B cell and $CD8^+$ T cell infiltration in HF tissues (Fig. 2C). Comparative analysis of immune-associated genes further indicated that certain cytokine-encoding genes were upregulated in HF sam-

ples, including the genes encoding IL-2, IL-6, IL-11, IL-18, IL-21, and IL-22 (Fig. 2D). Correlations between these immune-related genes and HF-related FRGs were also examined (Fig. 2E).

3.3 Establishment of FRG-Associated Heart Failure Molecular Subtypes

A consensus clustering strategy was next used to group HF patient samples based on the 62 identified HF-associated FRGs (Fig. 3A). Samples were separated into two groups based on the fact that the strongest intra-group and weakest inter-group connections were evident at a clustering variable (k) value of 2 in generated CDF curves (Fig. 3B,C). A subsequent principal component analysis (PCA) indicated that these two HF subtypes were distinct from one another based on gene expression profiles (Fig. 3D). Differences in the 62 HF-associated FRGs were also compared between these two subtypes of HF (Fig. 3E,F).

3.4 Comparison of Functional Differences among HF Subtypes

To clarify the biological differences between these HF patient clusters, a GSEA enrichment analysis was con-

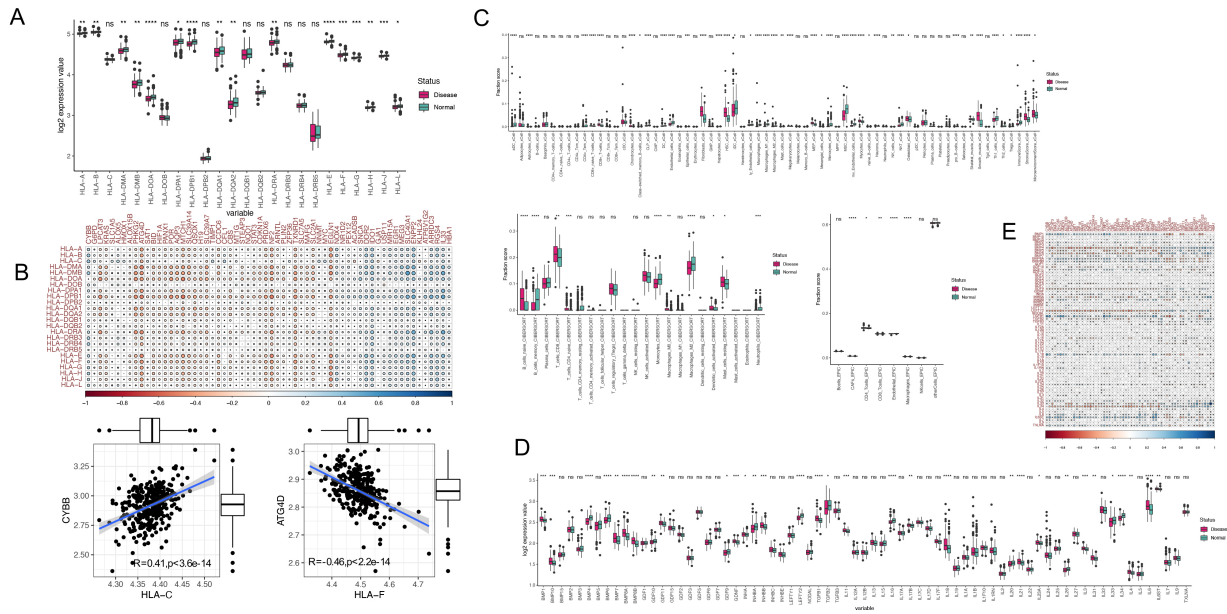


Fig. 2. The role of FRGs in immune regulation in heart failure. (A) Expression levels of HLA-related genes in disease and control samples. (B) Correlation analysis of HLA gene expression with FRGs in disease. (C) Immune cell infiltration analysis by XCell, CIBERSORT, and EPIC methods. (D) Expression levels of immune-associated genes in disease and healthy samples. (E) Correlation analysis of immune-associated genes and FRGs in disease samples (ns, not significant, *: <0.05, **: <0.01, ***: <0.001, ****: <0.0001).

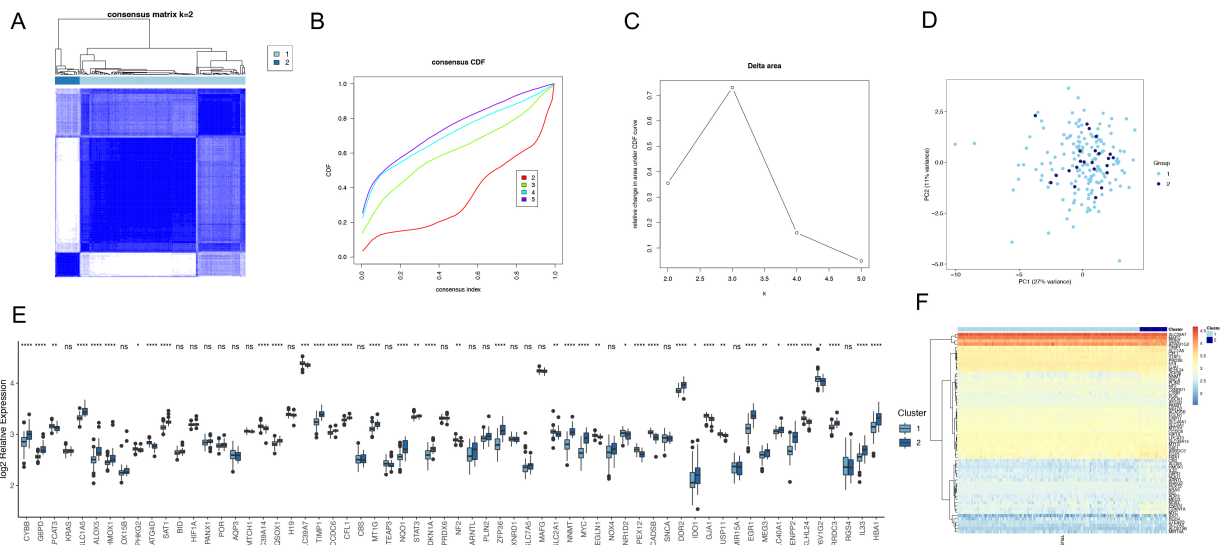


Fig. 3. Identification of FRGs-related molecular subtypes in heart failure. (A) Heat map showing the results of consistent cluster analysis for subtype identification. (B) The CDF value of consensus index. (C) Relative change in area under CDF curve for $k = 2-5$. (D) Principal component analysis showing the clustering of each disease sample according to subgroup groupings. (E) Box plot showing the distribution of FRGs expression according to subgroups, with the x-axis representing FRGs and the y-axis the logarithm of relative expression. (F) Heat map showing the expression of FRGs according to subgroups. (ns, not significant, *: <0.05, **: <0.01, ***: <0.001, ****: <0.0001). CDF, cumulative distribution function.

ducted for each of these subtypes. KEGG pathway enrichment analyses revealed that relative to samples in Cluster 1, those in Cluster 2 were more closely associated

with immune-associated pathways including the primary immunodeficiency, natural killer cell-mediated cytotoxicity, FcεRI signaling, and antigen processing and presen-

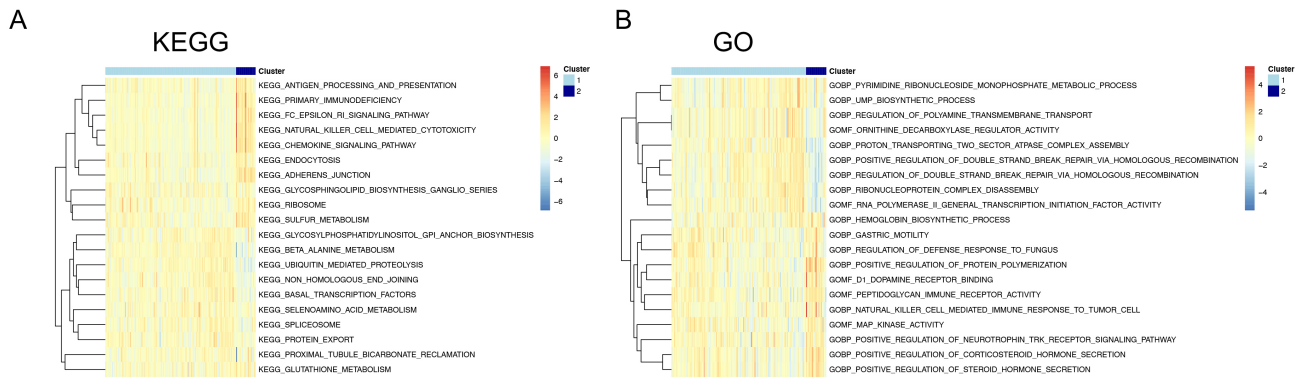


Fig. 4. Functional analysis of different molecular subtypes. (A) KEGG. (B) Gene Ontology.

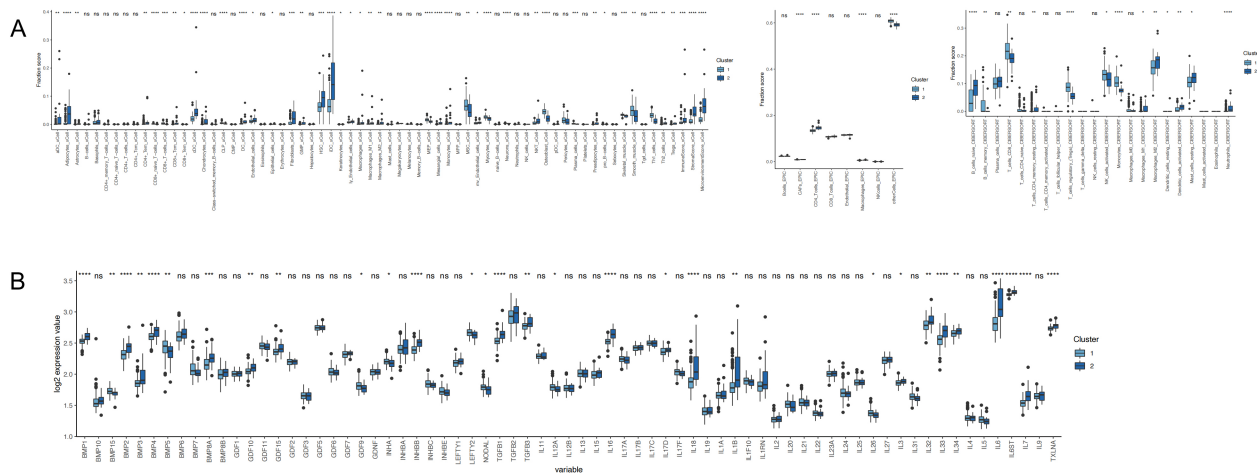


Fig. 5. Immune microenvironment of different molecular subtypes. (A) Analysis of immune infiltrating cells between subtypes. (B) Differences in expression of immune response genes between subtypes, ns: not significant, *: <math><0.05</math>, **: <math><0.01</math>, *: <math><0.001</math>, ****: <math><0.0001</math>.**

tation pathway (Fig. 4A). GO analyses similarly revealed the enrichment of immune-related functions including peptidoglycan immune receptor activity and natural killer cell-mediated immune responses to tumor cells in these HF patient clusters (Fig. 4B).

3.5 Examination of the Immune Microenvironment Associated with Different Subtypes of HF

The immunological microenvironment associated with these established HF patient subtypes was next explored by using three algorithms to assess immune cell infiltration in these patient samples. This approach revealed increased immune cell infiltration in samples from Subtype 2 relative to Subtype 1 (Fig. 5A). Moreover, Subtype 2 samples exhibited significant increases in the expression of immune-related genes including IL-6, IL-26, IL-18, TGFB1, and TGFB3 (Fig. 5B). These results highlight key differences in immune cell infiltration among these ferroptosis-associated HF patient subtypes, underscoring the close interplay between ferroptotic processes and the HF-related immune microenvironment.

3.6 Weighted Coexpression Network Establishment and Hub Gene Selection

A co-expression network was next developed based on the identified differentially expressed genes (DEGs) and HF patient cluster phenotypes in an effort to define gene modules significantly associated with these clusters. Differential gene expression analyses were initially performed among these clusters with established significant thresholds, revealing genes and functions that were distinct among these clusters (Fig. 6A–C). Interactions between these DEGs were then examined through the construction of a co-expression network (Fig. 6D,E). The DynamicTreeCut method revealed three total co-expression modules (Fig. 6F), and the modules that were most highly correlated were filtered based on cluster information. For example, the blue module from Cluster 2 was most strongly correlated with the turquoise module from Cluster 1 (Fig. 6E). Given the large numbers of genes in these modules, they were further assessed to identify hub genes of interest by calculating module feature vectors and their associations

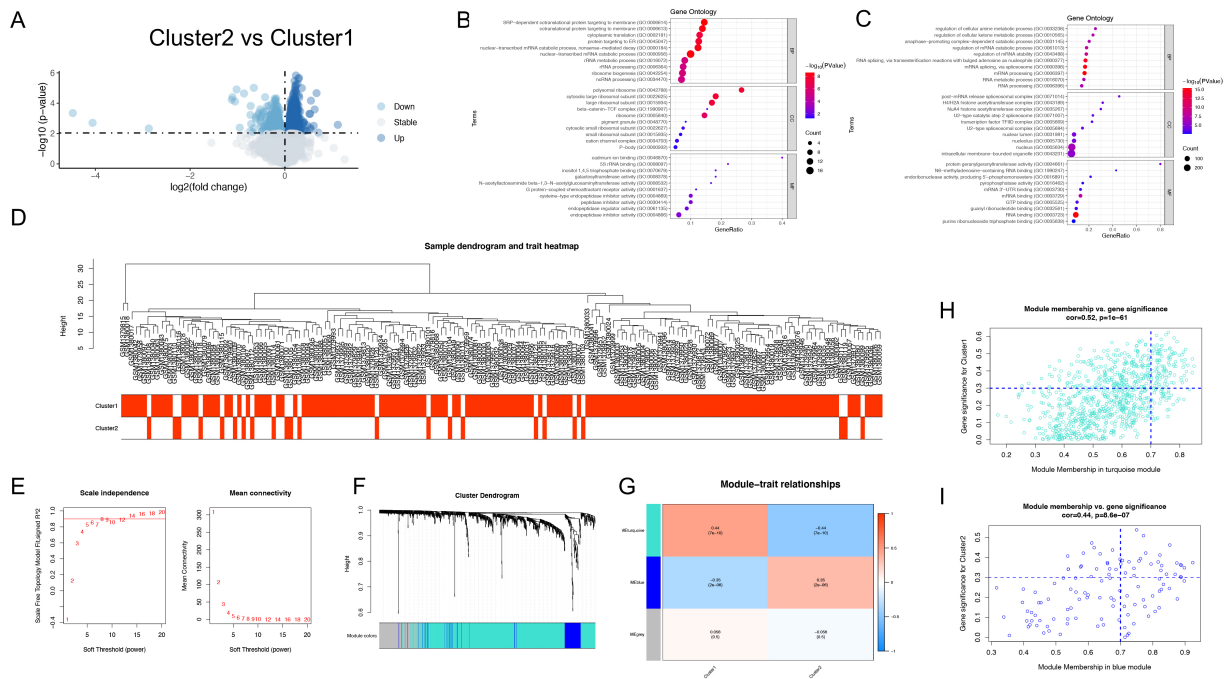


Fig. 6. Weighted Coexpression Network Construction and Identification of Hub genes. (A) Volcano plot showing the differential genes between clusters. (B,C) Functional analysis between two clusters. (D) Clustering of samples and removal of outliers. (E) Analysis of network topology for various soft-thresholding powers. (F) Cluster dendrogram of genes in all patients. Each branch in the figure represents one gene, and each color represents one coexpression module. (G) Correlation between the gene module and clusters. (H) The scatter plot of Gene significance vs. Module membership in the turquoise co-expression module. (I) The scatter plot of Gene significance vs. Module membership in the blue co-expression module.

with genes to define module membership (MM) and gene significance (GS). In total, 111 hub genes in Cluster1 and 32 hub genes in Cluster2 were identified based on established criteria ($GS > 0.3$ and $MM > 0.7$) (Fig. 6E,F, **Supplementary Tables 1,2**).

3.7 Candidate Drug Identification

Next, DGIdb was utilized to identify candidate drugs and compounds with the potential to treat HF based on the hub genes identified above. Accordingly, gene-drug interaction information was used to establish a protein-protein interaction network, with hub nodes in this network then being leveraged to determine candidate drugs of interest (Fig. 7A,B). In total, 27 drug candidates associated with 4 hub genes (HDAC1, LNPEP, PSMA1, and PSMA6) were identified (Fig. 7C). Of these compounds, 21 were predicted to interact with HDAC1, including abexinostat, an-9, apicidin, belinostat, cudc-101, and dacinostat.

3.8 In Vivo Validation of the Relevance of Four Hub Genes as Molecular Targets in HF

To confirm the *in vivo* relevance of the above findings, an *in vivo* model of HF was established by performing TAC surgery on C57BL/6 mice, with echocardiographic analyses of these animals being performed at 8 weeks post-surgery (Fig. 8A). These analyses revealed that LV EF and LV FS

were significantly reduced in mice in the TAC group relative to the sham control group (Fig. 8B), while the IVSd, LVIdD, and LVIdS were increased (Fig. 8C). Heart volume was also increased significantly in mice in the TAC surgery group (Fig. 8D). HE staining results also showed myocardial hypertrophy in the TAC group of mice, with a large number of disorganized cardiomyocytes, significantly increased cytoplasm, and extensive inflammatory cell infiltration (Fig. 8D). Meanwhile, WGA staining demonstrated a significantly larger ventricular cross-sectional area in TAC mice (Fig. 8E). Subsequently, we assessed myocardial interstitial and perivascular fibrosis in ventricular tissue in Masson-stained sections. As expected, TAC surgery promoted the progression of cardiac fibrosis (Fig. 8F). These results confirmed successful HF model establishment.

Based on the successful establishment of this model, we observed the changes of mitochondria in cardiomyocytes of TAC mice using transmission electron microscopy. The results showed that compared with the Sham group, the mitochondria in the cardiomyocytes of mice after TAC were apparently smaller, disordered in arrangement, with indistinct cristae and ruptured outer membranes (Fig. 8G). Meanwhile, we measured the ferrous ion content and the expression levels of ferroptosis-related factors MDA and GSH, and the results showed that the mice in the TAC group had obviously higher ferrous ion content and

The advent of new high-throughput sequencing technologies and other forms of so-called “big data”, however, has provided new opportunities to define key molecular correlates for HF development. The immune microenvironment is thought to play a pathological role in the onset of HF [18]. Environmental risk factors can increase the production of reactive oxygen species caused by oxidative stress, which in turn induces ferroptosis in cells [19], and the close relationship between the immune microenvironment and ferroptosis has been demonstrated in many fields, including oncology. As such, this study was developed to explore correlations between ferroptotic cell death and HF in an effort to provide a new foundation for the immunotherapeutic treatment of patients suffering from this condition.

Here, possible relationships between HF and ferroptosis were explored by comparisons of HF patient and control tissue samples, ultimately leading to the identification of 62 FRGs that were differentially expressed in HF samples (41 upregulated, 20 downregulated). Analyses of the immune microenvironment in these samples revealed the significant downregulation of most HLA genes in HF patient samples with corresponding increases in B cell and $CD8^+$ T cell infiltration in these samples and the concomitant upregulation of cytokine genes encoding *IL-2*, *IL-6*, *IL-11*, *IL-18*, *IL-21*, and *IL-22*. These HF-related FRGs were then used to group HF patient samples into two clusters, and differences in the makeup of the immune microenvironment were compared between these samples. Pathway enrichment analyses indicated that relative to Cluster1, Cluster 2 was primarily associated with the immune-related primary immunodeficiency, natural killer cell-mediated cytotoxicity, FcεRI signaling, and antigen processing and presentation pathways. Consistently, GO analyses revealed the enrichment of peptidoglycan immune receptor activity and natural killer cell-mediated immune response to tumor cells in these clusters. Significant differences in immune cell infiltration was observed when comparing these two clusters, with higher levels of such infiltration in Cluster2 relative to Cluster1. Moreover, Cluster2 exhibited the upregulation of immune-related genes encoding *IL-16*, *IL-18*, *IL-26*, *TGFB1*, and *TGFB3*. This approach revealed key differences in immune-associated genes and cell types related to ferroptosis, emphasizing a key role that ferroptosis plays in shaping the HF-related immunological microenvironment. A co-expression network based on identified DEGs was then established, with further analyses leading to the selection of 111 and 32 hub genes in Cluster1 and Cluster2, respectively.

Using DGIdb, candidate drugs capable of treating HF that targeted the HDAC1, LNPEP, PSMA1, and PSMA6 hub genes were also identified, offering promising tools that may aid in the future clinical management of affected patients. Several previous studies have shown that HDAC1, LNPEP, PSMA1 and PSMA6 are closely associated with ferroptosis and heart failure. Zhang *et al.* [20] found that

Yixinshu capsules improve cardiac hypertrophy by modulating the RB/HDAC1/GATA4 signaling pathway based on proteomics and mass spectrometry image analysis. Meanwhile, it has been indicated that CaMKII can exacerbate the progression of heart failure by activating class I HDAC [21]. Overexpression of PI16 reduced nuclear levels of HDAC1 after angiotensin II treatment, and overexpression of PI16 prevented cardiac hypertrophy and fibrosis by inhibiting stress-induced CF activation [22]. In addition, Huang *et al.* [23] identified ferroptosis in glomerular intrinsic cells of diabetic nephropathy patients with a potential key candidate gene, ALOX15, which may be regulated by HDAC1 and E3 ligase-related regulation. Emerging evidence suggests that differentially expressed protein and WGCNA analysis identified 18 upregulated proteins in non-ischemic dilated cardiomyopathy (DCM), including PSMA3 and PSMA6 [24].

To confirm the *in vivo* relevance of the above findings, an *in vivo* model of HF was established by performing TAC surgery on C57BL/6 mice. Our results revealed that LVEF and LVFS were significantly reduced in mice in the TAC group relative to the sham control group, while the IVSd, LVIDd, and LVIDs were increased. Heart volume was also increased significantly in mice in the TAC surgery group. The same was demonstrated for HE and WGA staining, while Masson staining verified significant fibrosis of cardiomyocytes in mice with heart failure. These results confirmed successful HF model establishment. Numerous studies have shown that ferroptosis plays an important role in the development of HF [4]. Excess intracellular iron can trigger ferroptosis by increasing reactive oxygen species levels through the Fenton reaction, promoting lipid peroxidation, and producing oxidation products that are highly toxic to cells, such as malondialdehyde (MDA). Secondly, it has been shown that excess intracellular free iron can enter mitochondria and promote mitochondrial oxidative stress, leading to cardiac mitochondrial dysfunction and GSH depletion. Consistent with these findings, we detected typical cardiomyocyte ferroptosis phenotypes such as elevated MDA and ferrous ion concentrations, decreased GSH expression and smaller mitochondrial volume and mitochondrial cristae crinkling in TAC-induced heart failure mice.

Subsequent qPCR and western blot analysis revealed that HDAC1, LNPEP, PSMA1 and PSMA6 expression differed significantly between these two groups of mice in line with the above results from bioinformatics analyses, again supporting a possible relationship between ferroptosis and HF. It also provides a rationale for its use as a potential heart failure-related biomarker, which will likely be a therapeutic strategy to stop the progression of heart failure in the future. This study also has some limitations. It simply verified the changes in gene expression. However, their specific functional validation and mechanism of action still need further study.

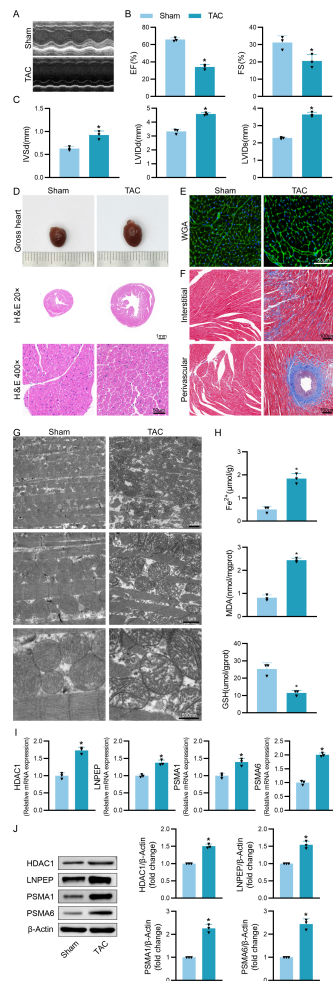


Fig. 8. Validation of the four hub genes expressions in animal models. (A–C) Mice in the indicated groups underwent M-mode echocardiographic imaging to assess left ventricle parameters in the long axis of the left parasternal sternum. Analyzed parameters included ejection fraction (EF), fractional shortening (FS), left ventricular internal diastolic diameter (LVIDd), left ventricular internal diameter end-systole (LVIDs), and interventricular septal dimension in diastole (IVSd). (D) Representative of gross cardiac morphology and H&E-stained cross-sections (20× and 400×). (E) WGA staining and cell surface area analyses of cardiomyocyte cross-sectional area (CSA). (F) Representative images of interstitial and perivascular myocardial fibrosis in the ventricular sections. (G) Representative images of the ultrastructural morphological characteristics of cardiomyocyte mitochondria. (H) Iron, malondialdehyde (MDA), and glutathione (GSH) levels in murine cardiomyocytes were quantified with appropriate commercial kits. (I) The relative expressions of HDAC1, LNPEP, PSMA1 and PSMA6 were assessed via qPCR in cardiomyocytes. (J) Representative Western immunoblots with corresponding quantification assessing HDAC1, LNPEP, PSMA1 and PSMA6 levels in cardiomyocytes. Data are means ± SEM. * $p < 0.05$. $n = 3/\text{group}$. Statistical differences between two groups were determined by Student's t -test. WGA, wheat germ agglutinin; H&E, hematoxylin-eosin; qPCR, quantitative polymerase chain reaction.

In summary, the present study offers new foundational insights regarding the relationship between ferroptosis and HF. To our knowledge, these analyses represent a new direction to investigate the link between the immune microenvironment and ferroptosis in heart failure patients, and the resulting data will drive future efforts to better treat this debilitating disease and improve patient survival and quality of life.

5. Conclusions

The importance of ferroptosis as a regulator of the immune microenvironment associated with HF was confirmed by bioinformatics analysis between ferroptosis and the immune microenvironment. Four related central genes, *HDAC1*, *LNPEP*, *PSMA1* and *PSMA6*, were identified to provide new strategies for individualized treatment of HF.

Availability of Data and Materials

The original data supporting the conclusions of this paper will be provided by the authors without reservation.

Author Contributions

JZ, JS and PX performed the main experiments. GW, CW and JL contributed to collection and assembly of data. HS and WY performed statistical analysis of all data. QL contributed to conception, supervision, administration, and validation of this project. All authors contributed to editorial changes in the manuscript. All authors read and approved the final manuscript. All authors have participated sufficiently in the work and agreed to be accountable for all aspects of the work. All authors reviewed the manuscript.

Ethics Approval and Consent to Participate

All experiments involving animals were approved by the Animal Ethics Committee of Nantong University. (Permit Number: S20220310-010).

Acknowledgment

Not applicable.

Funding

This work was supported by the grants from the Nantong Science and Technology Project (No. JC2021140).

Conflict of Interest

The authors declare no conflict of interest.

Supplementary Material

Supplementary material associated with this article can be found, in the online version, at <https://doi.org/10.31083/j.fbl2810246>.

References

- [1] Groenewegen A, Rutten FH, Mosterd A, Hoes AW. Epidemiology of heart failure. *European Journal of Heart Failure*. 2020; 22: 1342–1356.
- [2] Braunwald E. Biomarkers in Heart Failure. *New England Journal of Medicine*. 2008; 358: 2148–2159.
- [3] McDonagh TA, Metra M, Adamo M, Gardner RS, Baumbach A, Böhm M, *et al.* 2021 ESC Guidelines for the diagnosis and treatment of acute and chronic heart failure. *European Heart Journal*. 2021; 42: 3599–3726.
- [4] Magnussen C, Blankenberg S. Biomarkers for heart failure: small molecules with high clinical relevance. *Journal of Internal Medicine*. 2018; 283: 530–543.
- [5] Cao JY, Dixon SJ. Mechanisms of ferroptosis. *Cellular and Molecular Life Sciences*. 2016; 73: 2195–2209.
- [6] Yagoda N, von Rechenberg M, Zaganjor E, Bauer AJ, Yang WS, Fridman DJ, *et al.* RAS–RAF–MEK-dependent oxidative cell death involving voltage-dependent anion channels. *Nature*. 2007; 447: 865–869.
- [7] Shen Z, Song J, Yung BC, Zhou Z, Wu A, Chen X. Emerging Strategies of Cancer Therapy Based on Ferroptosis. *Advanced Materials*. 2018; 30: e1704007.
- [8] Stockwell BR, Friedmann Angeli JP, Bayir H, Bush AI, Conrad M, Dixon SJ, *et al.* Ferroptosis: A Regulated Cell Death Nexus Linking Metabolism, Redox Biology, and Disease. *Cell*. 2017; 171: 273–285.
- [9] Liang C, Zhang X, Yang M, Dong X. Recent Progress in Ferroptosis Inducers for Cancer Therapy. *Advanced Materials*. 2019; 31: 1904197.
- [10] Jennis M, Kung CP, Basu S, Budina-Kolomets A, Leu JI, Khaku S, *et al.* An African-specific polymorphism in the TP53 gene impairs p53 tumor suppressor function in a mouse model. *Genes & Development*. 2016; 30:918–930.
- [11] Tsai Y, Xia C, Sun Z. The Inhibitory Effect of 6-Gingerol on Ubiquitin-Specific Peptidase 14 Enhances Autophagy-Dependent Ferroptosis and Anti-Tumor *in vivo* and *in vitro*. *Frontiers in Pharmacology*. 2020; 11: 598555.
- [12] Hajibabaie F, Kouhpayeh S, Mirian M, Rahimmanesh I, Bosh-tam M, Sadeghian L, *et al.* MicroRNAs as the actors in the atherosclerosis scenario. *Journal of Physiology and Biochemistry*. 2020; 76: 1–12.
- [13] Hajibabaie F, Abedpoor N, Safavi K, Taghian F. Natural remedies medicine derived from flaxseed (secoisolaricresinol diglucoside, lignans, and α -linolenic acid) improve network targeting efficiency of diabetic heart conditions based on computational chemistry techniques and pharmacophore modeling. *Journal of Food Biochemistry*. 2022; 46: e14480.
- [14] Del Re DP, Amgalan D, Linkermann A, Liu Q, Kitsis RN. Fundamental Mechanisms of Regulated Cell Death and Implications for Heart Disease. *Physiological Reviews*. 2019; 99: 1765–1817.
- [15] Dixon S, Lemberg K, Lamprecht M, Skouta R, Zaitsev E, Gleason C, *et al.* Ferroptosis: An Iron-Dependent Form of Nonapoptotic Cell Death. *Cell*. 2012; 149: 1060–1072.
- [16] Lippi G, Sanchis-Gomar F. Global epidemiology and future trends of heart failure. *American Journal of Medicine*. 2020; 5: 5–15.
- [17] GBD 2017 Disease and Injury Incidence and Prevalence Collaborators. Global, regional, and national incidence, prevalence, and years lived with disability for 354 diseases and injuries for 195 countries and territories, 1990–2017: a systematic analysis for the Global Burden of Disease Study 2017. *Lancet*. 2018; 392: 1789–1858.
- [18] Pellicori P, Khan MJI, Graham FJ, Cleland JGF. New perspectives and future directions in the treatment of heart failure. *Heart Failure Reviews*. 2020; 25: 147–159.
- [19] Hajibabaie F, Aali F, Abedpoor N. Pathomechanisms of non-coding RNAs and hub genes related to the oxidative stress in diabetic complications. *F1000Research*. 2022; 11: 1132.
- [20] Zhang M, Guo F, Li X, Xian M, Wang T, Wu H, *et al.* Yi-Xin-Shu capsule ameliorates cardiac hypertrophy by regulating RB/HDAC1/GATA4 signaling pathway based on proteomic and mass spectrometry image analysis. *Phytomedicine*. 2022; 103: 154185.
- [21] Zhang M, Yang X, Zimmerman RJ, Wang Q, Ross MA, Granger JM, *et al.* CaMKII exacerbates heart failure progression by activating class I HDACs. *Journal of Molecular and Cellular Cardiology*. 2020; 149: 73–81.
- [22] Deng M, Yang S, Ji Y, Lu Y, Qiu M, Sheng Y, *et al.* Overexpression of peptidase inhibitor 16 attenuates angiotensin II-induced cardiac fibrosis via regulating HDAC1 of cardiac fibroblasts. *Journal of Cellular and Molecular Medicine*. 2020; 24: 5249–5259.
- [23] Huang G, Huang Z, Peng Y, Wang Y, Liu W, Xue Y, *et al.* Metabolic processes are potential biological processes distinguishing nonischemic dilated cardiomyopathy from ischemic cardiomyopathy: A clue from serum proteomics. *Pharmacogenomics and Personalized Medicine*. 2021; 14: 1169–1184.
- [24] Wang X, Jiang L, Liu XQ, Huang YB, Zhu W, Zeng HX, *et al.* Identification of Genes Reveals the Mechanism of Cell Ferroptosis in Diabetic Nephropathy. *Frontiers in Physiology*. 2022; 13: 890566.